PHYSICAL REVIEW B **108**, 035140 (2023)

Nonlinear Hall effect and potential Ising superconductivity in monolayer MXene heterostructure of T-Mo$_2$C/H-Mo$_2$C

Ning-Ning Zhao,[1] Zhen-Feng Ouyang,[1] Pei-Han Sun,[1] Jian-Feng Zhang,[2] Kai Liu,[1,3,*] and Zhong-Yi Lu[1,3,†]
[1]*Department of Physics and Beijing Key Laboratory of Opto-electronic Functional Materials & Micro-nano Devices,*
Renmin University of China, Beijing 100872, China
[2]*Institute of Physics, Chinese Academy of Sciences, Beijing 100190, China*
[3]*Key Laboratory of Quantum State Construction and Manipulation (Ministry of Education), Renmin University of China,*
Beijing, 100872, China

(Received 15 January 2023; accepted 6 July 2023; published 21 July 2023)

The Berry curvature dipole (BCD) induced nonlinear Hall effect can appear in a material with time-reversal symmetry but breaking space-inversion symmetry. Meanwhile, a two-dimensional (2D) noncentrosymmetric superconducting material can host exotic Ising pairing that leads to an upper critical magnetic field far exceeding the Pauli paramagnetic limit. Based on first-principles electronic structure calculations and theoretical analysis, we demonstrate that the large BCDs and the Ising superconductivity can coexist in the monolayer MXene heterostructures of T-Mo$_2$C/H-Mo$_2$C. The large BCDs are generated by the multiple band anticrossings and the band inversions near the Fermi level. The breaking of in-plane space-inversion symmetry in these 2D superconducting heterostructures can induce an Ising-type spin-orbit coupling. Additionally, one of the superconducting heterostructures is identified as a Z_2 topological metal. Our work suggests that the T-Mo$_2$C/H-Mo$_2$C heterostructures may serve as a promising platform to explore the nonlinear Hall effect and potential Ising superconductivity.

DOI: 10.1103/PhysRevB.108.035140

I. INTRODUCTION

The heterostructures of two-dimensional (2D) materials have attracted increasing interest recently in the fields of electronic transport, superconductivity, topology, magnetism, etc. Owing to the interlayer hybridization, these heterostructures may exhibit novel physical properties such as topological superconductivity, the quantum anomalous Hall effect, the valley Hall effect, and so on [1–6]. Moreover, the stacking modes, twisted angles, and lateral sliding in the heterostructures can also affect the electronic structures and the related properties [7–9]. In addition to the heterostructures that usually consist of distinct materials, there are some heterostructures composed of the materials with the same chemical composition but different polymorphs [10]. Like transition metal dichalcogenides (TMDCs), the monolayer MXene material Mo$_2$C also has the octahedral (T) and trigonal prismatic (H) phases [11–13]. Given that bulk α-Mo$_2$C has been recently fabricated in thin flakes [14–16] and predicted to be a topological superconductor candidate [17], we are curious about the transport and superconducting properties of the MXene heterostructures constructed with the T-Mo$_2$C and H-Mo$_2$C monolayers.

The Hall conductance is often adopted to characterize the transport properties of various materials including the 2D heterostructures. In the linear response regime, where the transverse Hall voltage is linearly proportional to the longitudinal driving current, the nonzero Hall conductance or the anomalous Hall conductance requires the time-reversal symmetry to be broken by an external magnetic field or the internal magnetization [18]. However, in the nonlinear response regime, the transverse Hall currents that are quadratic with the driving electric field can appear in the presence of time-reversal symmetry but with breaking of space-inversion symmetry [19–22]. This second-order response to the incident electric field is called the nonlinear Hall effect, which originates from the dipole moment of Berry curvature in the momentum space [19]. The nonlinear Hall effect can be utilized in nonlinear quantum devices for energy harvesting, wireless communications, and infrared detectors [23]. From the material point of view, noncentrosymmetric topological materials or systems are appropriate candidates to host such nonlinear Hall conductance due to the large Berry curvature dipoles (BCDs) induced by the nontrivial electronic structures [24–38]. Meanwhile, topologically trivial systems, such as the Bi(100) monolayer/NbSe$_2$ heterostructure and monolayer 2H-type TMDCs [39–44], can also generate nonzero BCDs, even though their values are often small due to there being few band crossings near the Fermi level.

On the other hand, noncentrosymmetric 2D materials or systems may also have intriguing superconducting properties. The 2H-type superconducting TMDCs such as gated MoS$_2$ and NbSe$_2$ are deemed to be type-I Ising superconductors with strongly enhanced in-plane upper critical magnetic fields [45–48]. This enhancement occurs because the Ising-type spin-orbit coupling (SOC) gives rise to an effective Zeeman field, which pins the electron spins to the out-of-plane direction and thus leads to an in-plane upper

---

[*] kliu@ruc.edu.cn
[†] zlu@ruc.edu.cn

critical field that is far beyond the Pauli paramagnetic limit [49–51]. Additionally, the few-layer $1T_d$-MoTe$_2$ exhibits a large in-plane upper critical field with an emergent twofold symmetry, which is different from the isotropic critical field in $2H$-type TMDCs [52]. However, most 2D superconductors have inversion symmetry and cannot generate the Zeeman-protected superconductivity. Thus noncentrosymmetric heterostructures may provide a new strategy to realize such Ising superconductivity.

Here, we theoretically construct two types of monolayer MXene heterostructures of T-Mo$_2$C/H-Mo$_2$C. Based on the first-principles electronic structure calculations, large BCDs in these T-Mo$_2$C/H-Mo$_2$C heterostructures can be induced by the multiple band anticrossings near the Fermi level with an in-plane tensile strain, which could generate nonlinear Hall conductance. In addition, these two heterostructures are predicted to be superconducting with the respective critical temperatures T_c of 12 and 8 K. Given the inversion asymmetry of these heterostructures, a large in-plane upper critical field can be sustained under the protection of the Ising-type SOC. Besides, one of the heterostructures is found to possess nontrivial topological properties [53]. Our calculations thus uncover a promising system with nonlinear Hall effect and potential Ising superconductivity.

II. METHOD

The electronic structures and the transport properties of the MXene heterostructures of T-Mo$_2$C/H-Mo$_2$C were studied based on the first-principles electronic structure calculations [54]. The projector augmented wave (PAW) method [55] as implemented in the Vienna *ab initio* simulation package (VASP) [56,57] was used to describe the core electrons as well as the interaction between the core and the valence electrons. The generalized gradient approximation (GGA) [58] of Perdew-Burke-Ernzerhof type was adopted for the exchange correlation functional. The kinetic energy cutoff of the plane-wave basis was set to be 520 eV. A 19 × 19 × 1 k-point mesh for Brillouin zone (BZ) sampling and the Gaussian smearing method with a width of 0.05 eV for Fermi surface broadening were utilized. A vacuum region larger than 20 Å is applied to avoid the interactions between adjacent slabs. The van der Waals interactions between the adjacent layers are taken into account by using the density functional theory with dispersion correction method DFT-D2 proposed by Grimme [59]. Both the shape of the slabs and the internal atomic positions were fully relaxed until the forces on all atoms were smaller than 0.01 eV/Å. Once the equilibrium structures were obtained, the electronic structures were further studied with the inclusion of the SOC effect. In order to explore the nontrivial topological properties and the Berry curvature dipole [60], the tight-binding Hamiltonian was constructed with the maximally localized Wannier functions [61–63] for the outmost s, p, and d orbitals of Mo atoms and the outmost s and p orbitals of C atoms generated by the first-principles calculations. A **k**-point grid of 2000 × 2000 × 1 was used in the integral Berry curvature dipole calculation to get a convergent result. The topological properties and edge states were studied by using the WANNIERTOOLS package [64].

When applying an ac electric field $E(t) = \mathrm{Re}\{\mathcal{E}_c e^{i\omega t}\}$, the nonlinear Hall current J_a can be generated with the rectified current part J_a^0 and double-frequency component $J_a^{2\omega}$ as [19]

$$J_a = \mathrm{Re}\{J_a^0 + J_a^{2\omega} e^{i2\omega t}\}, \tag{1}$$

where $J_a^0 = \chi_{abc}\mathcal{E}_b\mathcal{E}_c^*$ and $J_a^{2\omega} = \chi_{abc}\mathcal{E}_b\mathcal{E}_c$. In a time-reversal-symmetric system, the nonlinear Hall conductivity tensor χ_{abc} can be written as

$$\chi_{abc}(\omega) = -\varepsilon_{adc}\frac{e^3\tau}{2\hbar^2(1+i\omega\tau)}D_{bd}, \tag{2}$$

where ε_{adc} is the rank-3 Levi-Civita symbol and τ is the relaxation time. In experiment, the frequency ω and relaxation time τ are approximately 10–1000 Hz and in the range of picoseconds, respectively, which leads to $\omega\tau \ll 1$. Thus the nonlinear Hall conductance is independent of the frequency and mainly originates from the Berry curvature dipole D_{bd}, which can be expressed as

$$\begin{aligned} D_{bd} &= \sum_n \int_{\mathbf{k}} f_{n\mathbf{k}} \frac{\partial \Omega^d_{n\mathbf{k}}}{\partial \mathbf{k}_b} \\ &= \sum_n \int_{\mathbf{k}} \frac{\partial \epsilon_{\mathbf{k}_n}}{\partial \mathbf{k}_b}\Omega^d_{n\mathbf{k}}\frac{\partial f_{n\mathbf{k}}}{\partial \epsilon_{\mathbf{k}_n}}, \end{aligned} \tag{3}$$

where $f_{n\mathbf{k}}$ is the Fermi-Dirac distribution function, n is the index of the occupied bands, and $\Omega^d_{n\mathbf{k}}$ is the Berry curvature. It is worth noting that only the z component of the Berry curvature survives in the 2D system, namely, $\Omega^z_{n\mathbf{k}}$,

$$\Omega^z_{n\mathbf{k}} = -\sum_{m\neq n}\frac{2\,\mathrm{Im}\langle\psi_{n\mathbf{k}}|v_x|\psi_{m\mathbf{k}}\rangle\langle\psi_{m\mathbf{k}}|v_y|\psi_{n\mathbf{k}}\rangle}{(\epsilon_{m\mathbf{k}}-\epsilon_{n\mathbf{k}})^2}, \tag{4}$$

where $\epsilon_{n\mathbf{k}}$ is the eigenvalue of the nth eigenstate $\psi_{n\mathbf{k}}$ and $v_i = \frac{1}{\hbar}\frac{\partial \epsilon_{\mathbf{k}}}{\partial \mathbf{k}_i}$ is the velocity operator along the i ($i = x, y$) direction.

The superconducting properties were studied based on the anisotropic Migdal-Eliashberg theory as implemented in the EPW code [65–67]. The d orbitals of Mo atoms and p orbitals of C atoms were considered to construct the maximally localized Wannier functions (MLWFs) [63]. The convergent electron-phonon coupling (EPC) constant λ was obtained with the fine electron (72 × 72 × 1) and phonon (24 × 24 × 1) grids. The Dirac δ functions for the electron and phonon parts were smeared out by the Gaussian function with widths of 50 and 0.5 meV, respectively. A fine electron grid of 72 × 72 × 1 points was employed when solving the anisotropic Eliashberg equations. The sum over the Matsubara frequencies was truncated with $\omega_c = 0.9$ eV, about ten times the highest phonon frequency.

III. RESULTS

A. Crystal structure and topological properties

The monolayer MXene of Mo$_2$C forms a layered structure in which the C layer is sandwiched between two Mo layers. The Mo$_2$C layers are stacked in an ABC sequence in the T phase (space group $P\bar{3}m1$, No. 164) and in an ABA sequence in the H phase (space group $P\bar{6}m2$, No. 187). For these T and H phases, the C atoms are located in the centers of Mo octahedra and Mo triangular prisms, respectively.

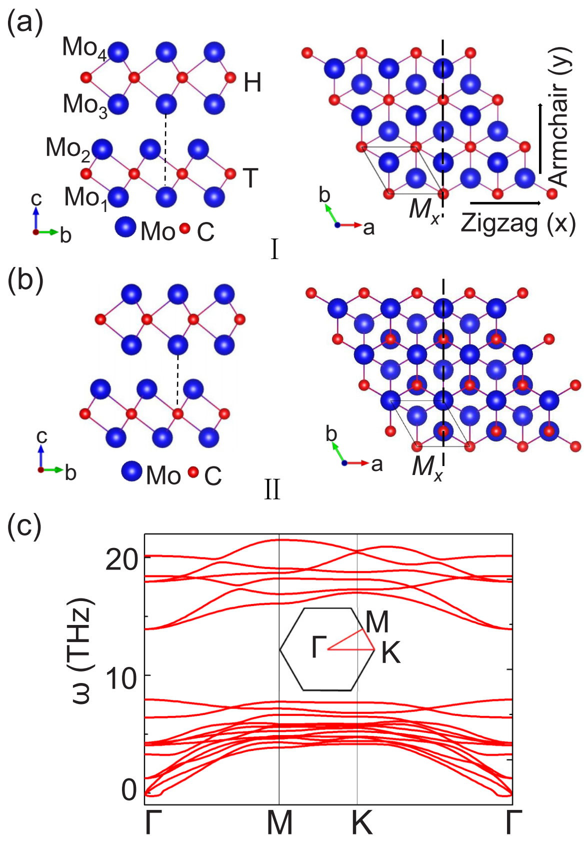

FIG. 1. (a) and (b) Top and side views of the T-Mo$_2$C/H-Mo$_2$C MXene heterostructures I and II. (c) Phonon spectra of the heterostructure I. Inset: two-dimensional (2D) Brillouin zone (BZ) with the red lines indicating the high-symmetry paths.

In order to study the nonlinear Hall effect, the inversion symmetry should be broken, and the multiple band crossings are expected near the Fermi level. Thus we construct several heterostructures of T-Mo$_2$C/H-Mo$_2$C based on the relative positions of Mo atoms in the H-Mo$_2$C layer above the T-Mo$_2$C layer (Fig. S1 in the Supplemental Material (SM) [68]). According to the calculated relative energies (Table S1 in the SM [68]), heterostructure II was found to be the ground state [Fig. 1(b)], while heterostructure I [Fig. 1(a)] was identified as a metastable state, with an energy difference of 200 meV per unit cell. Since both the T-Mo$_2$C monolayer and the H-Mo$_2$C monolayer have been synthesized and the interlayer sliding between the layers of bilayer T-Mo$_2$C has been reported in experiments [13], the heterostructure I of T-Mo$_2$C/H-Mo$_2$C may also be fabricated by sliding the H-Mo$_2$C layer in heterostructure II along the Mo armchair direction of the T-Mo$_2$C layer. Moreover, because the heterostructure I exhibits larger Berry curvature dipoles with lower doping levels and higher superconducting T_c than those of heterostructure II, we mainly discuss the properties of heterostructure I in the following. The optimized in-plane lattice constant of heterostructure I is $a = 2.906$ Å with an interlayer distance $d = 2.371$ Å, and those of heterostructure II are $a = 2.882$ Å and $d = 2.378$ Å. The corresponding 2D Brillouin zone (BZ) along with the high-symmetry k points is shown in the inset of Fig. 1(c). The main panel of Fig. 1(c) exhibits the calculated phonon dispersions of heterostructure I, indicating its dynamical stabilities.

Figures 2(a) and 2(b) display the electronic band structures of T-Mo$_2$C/H-Mo$_2$C heterostructure I along the high-symmetry BZ paths calculated without and with SOC, respectively. From the result without SOC, we can see that there are several bands crossing the Fermi level, mainly coming from the d orbitals of Mo atoms [Fig. 2(d)]. These bands form several band anticrossings due to the interlayer hybridization, which imply that heterostructure I may have nontrivial topological properties. Figure 2(c) shows the Dirac point [indicated by a blue circle in Fig. 2(a)] formed between the highest valence band and the lowest conduction band around the Fermi level in the absence of SOC. Once the SOC effect is turned on, the band anticrossings near the Fermi level open a continuous band gap through the whole BZ. We can thus define the topological invariant Z_2 between two adjacent gapped bands. By using the Wilson loop method [69], we obtain the topological invariant $Z_2 = 1$ in the region ±1 eV around the Fermi level as shown in Fig. 2(b), which indicates that heterostructure I is a topological metal [70,71]. The topological edge states are located in the projected bulk band gap and are not buried by bulk states at $E_F - 0.3$ eV (see Fig. S2 in the SM [68]). Additionally, we find that heterostructure II is topologically trivial (see Fig. S3 in the SM [68]). The distinct topological properties of these two heterostructures stem from the different orbital weights of their crossing bands.

B. Berry curvature dipole and nonlinear Hall effect

Due to the breaking of inversion symmetry in the T-Mo$_2$C/H-Mo$_2$C heterostructures, nonvanishing Berry curvatures are allowed in the momentum space [19]. More importantly, the gapped multiple band crossings near the Fermi level may give rise to large Berry curvatures [24]. In Fig. 2(b), the red solid line represents the calculated **k**-resolved Berry curvature $\Omega_z(\mathbf{k})$ at $E_F - 0.03$ eV along the high-symmetry paths of the BZ. As expected, a giant Berry curvature peak appears at the gapped Dirac point [the blue circle in Fig. 2(a)]. We have also calculated the distribution of the Berry curvature in the whole BZ. From Fig. 3, we can see that there are other gapped band crossing points near the E_F along the Γ-M and Γ-K lines that also have large contributions to the Berry curvature. Interestingly, the Berry curvatures satisfy $\Omega_z(k_x, k_y) = -\Omega_z(-k_x, -k_y)$ enforced by the time-reversal symmetry.

The positive and negative Berry curvature peaks in the 2D BZ may induce finite BCDs [44]. However, the BCDs in the strain-free T-Mo$_2$C/H-Mo$_2$C heterostructures become vanishing due to the following reason. The symmetry group of the two heterostructures of Mo$_2$C is C_{3v}, with generator operators C_{3z} and M_x. Under the operation of C_{3z}, their velocities v_x and v_y satisfy $v_x(\mathbf{k}) + v_x(C_{3z}^{+}\mathbf{k}) + v_x(C_{3z}^{-}\mathbf{k}) = 0$, $v_y(\mathbf{k}) + v_y(C_{3z}^{+}\mathbf{k}) + v_y(C_{3z}^{-}\mathbf{k}) = 0$, while the Berry curvature Ω_z satisfies $\Omega_z(\mathbf{k}) = \Omega_z(C_{3z}^{+}\mathbf{k}) = \Omega_z(C_{3z}^{-}\mathbf{k})$. Hence based on Eq. (3), the C_{3z} symmetry ensures the vanishment of D_{xz} and D_{yz} [42]. According to previous studies, the highest symmetry that allows a nonzero BCD in a 2D crystal is a single mirror line [20,41,43]. In order to observe the nonlinear Hall effect with a nonzero BCD, a uniaxial strain along the armchair (y)

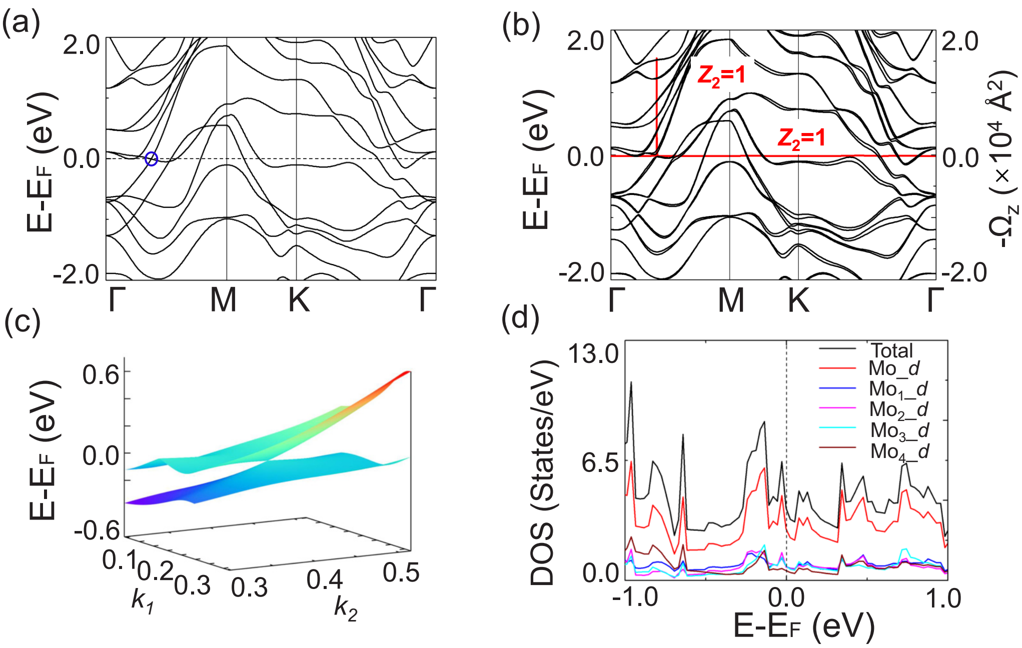

FIG. 2. Electronic band structures of heterostructure I calculated (a) without and (b) with the spin-orbital coupling (SOC) along the high-symmetry paths of the BZ. The red lines represent the calculated Berry curvature Ω_z at -0.03 eV below E_F. The topological invariants Z_2 are also labeled in the corresponding band gaps. (c) Three-dimensional (3D) band structure around the Dirac point indicated by the blue circle in (a). (d) Total and partial density of states (DOS) calculated without SOC.

or zigzag (x) direction should be introduced. This uniaxial in-plane strain reduces the symmetry from C_{3v} to C_{1h} with only one mirror line M_x preserved. Under the M_x symmetry, the Berry curvature Ω_z and velocity v_x are odd while the velocity v_y is even, namely, $\Omega_z(k_x, k_y) \rightarrow -\Omega_z(-k_x, k_y)$, $\frac{\partial\epsilon}{\partial k_x} \rightarrow -\frac{\partial\epsilon}{\partial k_x}$, $\frac{\partial\epsilon}{\partial k_y} \rightarrow \frac{\partial\epsilon}{\partial k_y}$. Thus, with a uniaxial in-plane strain, the BCD component D_{yz} vanishes while the D_{xz} can be finite.

Figure 4 exhibits the calculated BCD components D_{xz} of both T-Mo$_2$C/H-Mo$_2$C heterostructures (heterostructures I and II) under the tensile strains along the armchair and zigzag directions. Due to the gapped band anticrossings and the topological phase transitions (Fig. 2), the D_{xz} shows dramatic changes with the varying Fermi energy. As expected, the D_{xz} of heterostructure I varies rapidly and has multiple peaks above the Fermi level as shown in Figs. 4(a) and 4(b). Under 1% tensile strain along the armchair direction, the D_{xz} of heterostructure I [the blue line in Fig. 4(a)] has a relatively large value of 15 Å near the Fermi level, much higher than those of 2H-type TMDCs [39]. Remarkably, at $E_\mathrm{F} + 0.58$ eV, the value of D_{xz} reaches over 40 Å, which is comparable to that of the widely studied bilayer WTe$_2$ [25]. As shown in Figs. 4(c) and 4(d), heterostructure II also exhibits large D_{xz} by varying the Fermi energy, namely, doping of electrons or holes. In addition to the charge doping, the BCDs are also highly sensitive to the applied strain due to the dependence of the Berry curvature on the band structure.

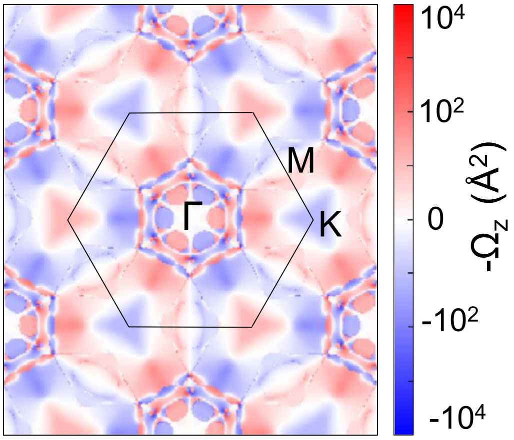

FIG. 3. The $\boldsymbol{k}$-resolved Berry curvature Ω_z of heterostructure I in the 2D BZ at $E_\mathrm{F} - 0.03$ eV. The red and blue colors indicate the positive and negative contributions, respectively.

With the large BCDs, an observable nonlinear Hall effect can be generated. According to Eq. (2), nonzero D_{xz} corresponds to nonvanishing nonlinear Hall coefficients χ_{xxy} and χ_{yxx}, which satisfy $\chi_{xxy} = -\chi_{yxx}$. When we apply an incident current, the driven second-order nonlinear Hall current density is expressed as $j_\perp^{2\omega} = e^3\tau/[2\hbar^2(1 + i\omega\tau)]|E|^2 D_{xz}\cos\theta$, where θ represents the angle between the direction of the incident current and the BCD [19,21,41]. In the strained T-Mo$_2$C/H-Mo$_2$C heterostructure, the BCD D_{xz} exists along the zigzag (x) direction perpendicular to the only mirror line M_x (Fig. 1). Thus the nonlinear Hall response reaches the maximum value when the incident current is parallel to the zigzag (x) direction.

C. Potential Ising superconductivity

According to previous studies, the bulk α-Mo$_2$C and monolayer T-Mo$_2$C and H-Mo$_2$C are electron-phonon-mediated superconductors [71–73]. We then studied the EPC superconductivity of the T-Mo$_2$C/H-Mo$_2$C heterostructures

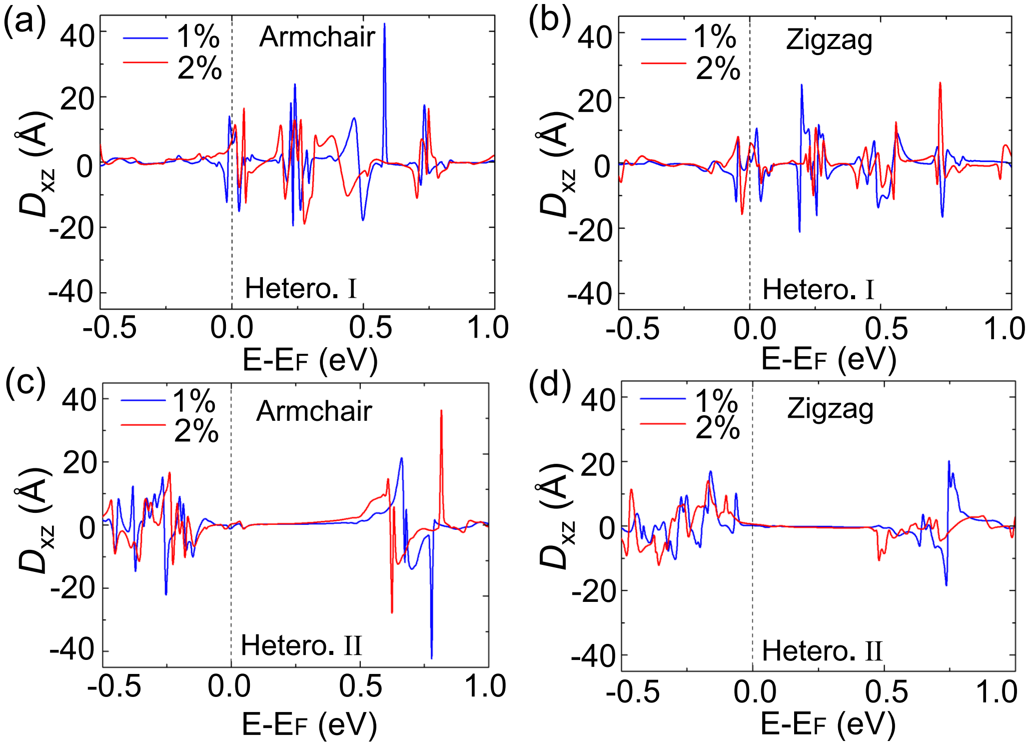

FIG. 4. The calculated BCD components D_{xz} as a function of energy under tensile strains along the armchair (y) and zigzag (x) directions for T-Mo$_2$C/H-Mo$_2$C heterostructure (hetero.) I [(a) and (b)] and heterostructure II [(c) and (d)].

based on the the anisotropic Migdal-Eliashberg theory [67]. The strengths of EPC were computed to be 0.98 and 0.74 for heterostructures I and II, respectively, of T-Mo$_2$C/H-Mo$_2$C. Figure 5 shows the normalized superconducting gap distributions at different temperatures for these two heterostructures. We can see that the superconducting gap for heterostructure I vanishes around 12 K, while heterostructure II exhibits a lower T_c of 8 K. This originates from a larger electronic density of states (DOS) at the Fermi level in heterostructure I than that in heterostructure II, which allows more electronic states to couple with the phonons.

For some monolayer 2H-type TMDCs that are called Ising superconductors, such as gated 2H-MoS$_2$, 2H-NbSe$_2$, and 2H-TaS$_2$, the in-plane upper critical field B_{c2} can exceed the Pauli paramagnetic limit by threefold to fivefold [45–48]. Due to the breaking of in-plane inversion symmetry, an Ising-type SOC pins the electron spins to the out-of-plane direction, which reduces the pair-breaking effect of the in-plane magnetic field and results in a large in-plane upper critical field. Thus the H-Mo$_2$C monolayer is also a promising candidate for an Ising superconductor.

In comparison to the case of the H-Mo$_2$C monolayer, in addition to the in-plane inversion asymmetry, the out-of-plane mirror symmetry in both T-Mo$_2$C/H-Mo$_2$C heterostructures (heterostructures I and II) is also broken due to the layer stacking. The absence of out-of-plane mirror symmetry results in a more complex spin polarization, which is similar to that in few-layer 1T_d-MoTe$_2$, a typical in-plane anisotropic Ising superconductor [44,52]. Figure 6(a) shows the distribution of the superconducting gap $\Delta_{n\mathbf{k}}$ on the Fermi surface for T-Mo$_2$C/H-Mo$_2$C heterostructure I at 5 K. On the whole Fermi surface, there are finite superconducting gaps. The

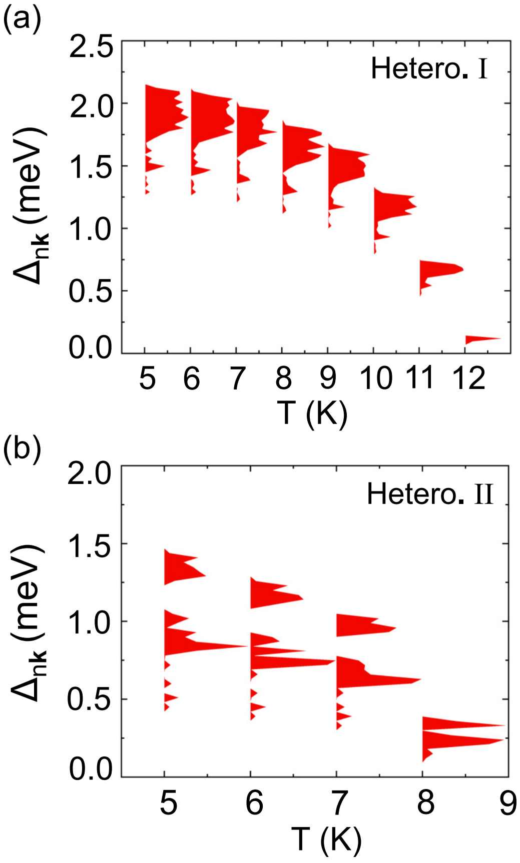

FIG. 5. Normalized superconducting gap distributions at different temperatures for T-Mo$_2$C/H-Mo$_2$C heterostructure I (a) and heterostructure II (b). The effective screened Coulomb repulsion constant μ^* is set to 0.1.

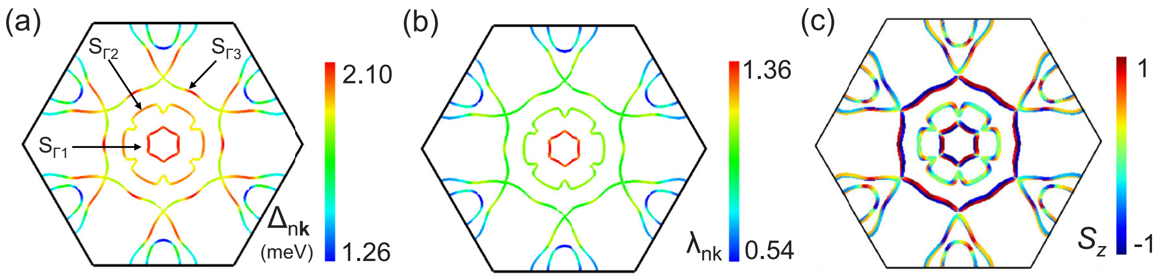

FIG. 6. (a) The distribution of the superconducting gap $\Delta_{n\mathbf{k}}$ on Fermi surfaces for T-Mo$_2$C/H-Mo$_2$C heterostructure I at 5 K. The screened Coulomb potential μ^* is set to 0.1. (b) The variation in electron-phonon coupling (EPC) on the Fermi surface; the colors stand for the EPC strength $\lambda_{\mathbf{k}n}$. (c) The spin polarization calculated with SOC along the S_z direction.

Fermi pocket $S_{\Gamma 1}$ exhibits the largest superconducting gap with 2.10 meV, and the Fermi pockets $S_{\Gamma 2}$ and $S_{\Gamma 3}$ have comparable superconducting gaps. In contrast, the superconducting gap on the Fermi pockets around the M points shows the smallest values. On the other hand, from the momentum-resolved EPC strengths on the Fermi surface [Fig. 6(b)], the Fermi pocket S_{Γ_1} exhibits the strongest EPC, which coincides with the distributions of the largest superconducting gap. In comparison to the spin polarization calculations [Fig. 6(c)], the Fermi pockets $S_{\Gamma 1}$ and $S_{\Gamma 3}$ with large superconducting gaps are precisely fully spin polarized along the out-of-plane direction. Similarly, the Fermi pockets around the Γ point (S_Γ) and the K point (S_K) at $E_F + 0.15$ eV for heterostructure II also show out-of-plane spin polarization; meanwhile, sizable EPC strengths and superconducting gaps are exhibited on the same pockets (see Fig. S4 in the SM [68]). Thus the in-plane upper critical field could be enhanced by the Cooper pairs formed by these electrons. The estimated Ising spin-orbit field $H_{\rm SOC}$ is $\Delta_{\rm SOC}/2\mu_B = 457.8$ T for heterostructure I, which is comparable to that of monolayer NbSe$_2$ [47]. Thus we propose that the T-Mo$_2$C/H-Mo$_2$C heterostructure could potentially be an Ising superconductor. Our theoretical proposals regarding T-Mo$_2$C/H-Mo$_2$C heterostructures need to be confirmed by future experimental studies.

IV. DISCUSSION AND SUMMARY

The emergence of the nonlinear Hall effect requires a nonvanishing BCD. So far, studies of the nonlinear Hall effect mainly include three kinds of materials: noncentrosymmetric topological materials such as ultrathin WTe$_2$ [26,27,33,38], some ferroelectric-like metals as LiOsO$_3$ [29,42], and some topological trivial materials [40,43,44]. However, experimental observations of the nonlinear Hall effect are mainly confined to 2D materials, while the reported 2D heterostructures that host sizable BCDs are very rare. In this paper, we theoretically construct two dynamically stable T-Mo$_2$C/H-Mo$_2$C heterostructures. The calculated BCD can reach over 40 Å at $E_F + 0.6$ eV under 1% uniaxial strain along the armchair direction in heterostructure I, which is comparable to that in bilayer WTe$_2$ and much higher than that in monolayer 2H-type TMDCs. As the H-Mo$_2$C and T-Mo$_2$C monolayers have been successfully fabricated and bilayer T-Mo$_2$C with different stacking orders has also been realized [13], the T-Mo$_2$C/H-Mo$_2$C heterostructures should be feasible in experiments. In addition, the piezoelectric substrate and the ionic-liquid gating voltage that can be used to apply the strain [43] and tune the Fermi level, respectively; thus the nonlinear Hall effect of the T-Mo$_2$C/H-Mo$_2$C heterostructures could be further modulated.

According to the EPC calculations, the superconducting T_c's for heterostructures I and II of T-Mo$_2$C/H-Mo$_2$C are estimated to be 12 and 8 K, respectively. Given the absence of inversion symmetry and the presence of a strong SOC effect, these heterostructures may host exotic Ising pairing, which can result in large in-plane upper critical magnetic fields beyond the Pauli paramagnetic limit [50]. Furthermore, our theoretical analysis reveals heterostructure I to be a Z_2 topological metal, whose edge states near the Fermi level can form the equivalent topological superconductivity via a proximity effect. Thus heterostructure I may also provide a playground for exploring topological superconductivity and the Majorana zero modes [74].

In summary, we have theoretically constructed two types of T-Mo$_2$C/H-Mo$_2$C heterostructures and then investigated their nonlinear Hall effects and superconducting properties. Based on our calculation results, the coexistence of large BCD and potential Ising pairing can be realized in the T-Mo$_2$C/H-Mo$_2$C heterostructures. The large BCD can induce a significant nonlinear Hall effect, while the potential Ising superconductivity can sustain a large in-plane upper critical field. As the H-Mo$_2$C and T-Mo$_2$C monolayers have been successfully fabricated, the predicted exotic properties could be realized by experiments in the future. Therefore the T-Mo$_2$C/H-Mo$_2$C heterostructures provide an interesting playground for future experimental explorations of the nonlinear Hall effect, Ising superconductivity, and potential topological superconductivity.

ACKNOWLEDGMENTS

This work was supported by the National Key R&D Program of China (Grants No. 2019YFA0308603 and No. 2022YFA1403103), the Beijing Natural Science Foundation (Grant No. Z200005), and the National Natural Science Foundation of China (Grants No. 12174443 and No. 11934020). N.-N.Z. was supported by the Outstanding Innovative Talents Cultivation Funded Programs 2020 of Renmin University of China. Computational resources were provided by the Physical Laboratory of High Performance Computing at Renmin University of China and the Beijing Super Cloud Computing Center.

[1] M.-X. Wang, C. Liu, J.-P. Xu, F. Yang, L. Miao, M.-Y. Yao, C. Gao, C. Shen, X. Ma, X. Chen, Z.-A. Xu, Y. Liu, S.-C. Zhang, D. Qian, J.-F. Jia, and Q.-K. Xue, Science **336**, 52 (2012).

[2] H.-H. Sun, K.-W. Zhang, L.-H. Hu, C. Li, G.-Y. Wang, H.-Y. Ma, Z.-A. Xu, C.-L. Gao, D.-D. Guan, Y.-Y. Li, C. Liu, D. Qian, Y. Zhou, L. Fu, S.-C. Li, F.-C. Zhang, and J.-F. Jia, Phys. Rev. Lett. **116**, 257003 (2016).

[3] G. Xu, J. Wang, C. Felser, X.-L. Qi, and S.-C. Zhang, Nano Lett. **15**, 2019 (2015).

[4] Z. Huang, Y. Liu, K. Dini, Q. Tan, Z. Liu, H. Fang, J. Liu, T. Liew, and W. Gao, Nano Lett. **20**, 1345 (2020).

[5] J. Li, M. Rashetnia, M. Lohmann, J. Koo, Y. Xu, X. Zhang, K. Watanabe, T. Taniguchi, S. Jia, X. Chen, B. Yan, Y.-T. Cui, and J. Shi, Nat. Commun. **13**, 5134 (2022).

[6] M. Serlin, C. Tschirhart, H. Polshyn, Y. Zhang, J. Zhu, K. Watanabe, T. Taniguchi, L. Balents, and A. Young, Science **367**, 900 (2020).

[7] Y. Cao, V. Fatemi, S. Fang, K. Watanabe, T. Taniguchi, E. Kaxiras, and P. Jarillo-Herrero, Nature (London) **556**, 43 (2018).

[8] G. W. Kim and G. Kim, Appl. Surf. Sci. **586**, 152596 (2022).

[9] J. Li, H. Jin, Y. Wei, and H. Guo, Phys. Rev. B **103**, 125403 (2021).

[10] Z. Wang, Y.-Y. Sun, I. Abdelwahab, L. Cao, W. Yu, H. Ju, J. Zhu, W. Fu, L. Chu, H. Xu, and K. P. Loh, ACS Nano **12**, 12619 (2018).

[11] R. Meshkian, L.-Å. Näslund, J. Halim, J. Lu, M. W. Barsoum, and J. Rosen, Scr. Mater. **108**, 147 (2015).

[12] J. Jeon, Y. Park, S. Choi, J. Lee, S. S. Lim, B. H. Lee, Y. J. Song, J. H. Cho, Y. H. Jang, and S. Lee, ACS Nano **12**, 338 (2018).

[13] X. Zhao, W. Sun, D. Geng, W. Fu, J. Dan, Y. Xie, P. R. Kent, W. Zhou, S. J. Pennycook, and K. P. Loh, Adv. Mater. **31**, 1808343 (2019).

[14] C. Xu, L. Wang, Z. Liu, L. Chen, J. Guo, N. Kang, X.-L. Ma, H.-M. Cheng, and W. Ren, Nat. Mater. **14**, 1135 (2015).

[15] Z. Zhang, H. Gedeon, Z. Cheng, C. Xu, Z. Shao, H. Sun, S. Li, Y. Cao, X. Zhang, Q. Bian, L. Liu, Z. Liu, H.-M. Cheng, W. Ren, and M. Pan, Nano Lett. **19**, 3327 (2019).

[16] C. Xu, Z. Liu, Z. Zhang, Z. Liu, J. Li, M. Pan, N. Kang, H.-M. Cheng, and W. Ren, Adv. Mater. **32**, 2002825 (2020).

[17] N.-N. Zhao, P.-J. Guo, X.-Q. Lu, Q. Han, K. Liu, and Z.-Y. Lu, Phys. Rev. B **101**, 195144 (2020).

[18] N. Nagaosa, J. Sinova, S. Onoda, A. H. MacDonald, and N. P. Ong, Rev. Mod. Phys. **82**, 1539 (2010).

[19] I. Sodemann and L. Fu, Phys. Rev. Lett. **115**, 216806 (2015).

[20] Z. Du, H.-Z. Lu, and X. Xie, Nat. Rev. Phys. **3**, 744 (2021).

[21] C. Ortix, Adv. Quantum Technol. **4**, 2100056 (2021).

[22] C. Wang, Y. Gao, and D. Xiao, Phys. Rev. Lett. **127**, 277201 (2021).

[23] H. Isobe, S.-Y. Xu, and L. Fu, Sci. Adv. **6**, eaay2497 (2020).

[24] Z. Z. Du, C. M. Wang, H.-Z. Lu, and X. C. Xie, Phys. Rev. Lett. **121**, 266601 (2018).

[25] Q. Ma, S.-Y. Xu, H. Shen, D. MacNeill, V. Fatemi, T.-R. Chang, A. M. Mier Valdivia, S. Wu, Z. Du, C.-H. Hsu, S. Fang, Q. D. Gibson, K. Watanabe, T. Taniguchi, R. J. Cava, E. Kaxiras, H.-Z. Lu, H. Lin, L. Fu, N. Gedik *et al.*, Nature (London) **565**, 337 (2019).

[26] Y. Zhang, Y. Sun, and B. Yan, Phys. Rev. B **97**, 041101(R) (2018).

[27] Y. Zhang, J. van den Brink, C. Felser, and B. Yan, 2D Mater. **5**, 044001 (2018).

[28] S.-Y. Xu, Q. Ma, H. Shen, V. Fatemi, S. Wu, T.-R. Chang, G. Chang, A. M. M. Valdivia, C.-K. Chan, Q. D. Gibson, J. Zhou, Z. Liu, K. Watanabe, T. Taniguchi, H. Lin, R. J. Cava, L. Fu, N. Gedik, and P. Jarillo-Herrero, Nat. Phys. **14**, 900 (2018).

[29] J. I. Facio, D. Efremov, K. Koepernik, J.-S. You, I. Sodemann, and J. van den Brink, Phys. Rev. Lett. **121**, 246403 (2018).

[30] K. Kang, T. Li, E. Sohn, J. Shan, and K. F. Mak, Nat. Mater. **18**, 324 (2019).

[31] H. Wang and X. Qian, npj Comput. Mater. **5**, 119 (2019).

[32] S. Singh, J. Kim, K. M. Rabe, and D. Vanderbilt, Phys. Rev. Lett. **125**, 046402 (2020).

[33] D. Kumar, C.-H. Hsu, R. Sharma, T.-R. Chang, P. Yu, J. Wang, G. Eda, G. Liang, and H. Yang, Nat. Nanotechnol. **16**, 421 (2021).

[34] H. Jin, H. Su, X. Li, Y. Yu, H. Guo, and Y. Wei, Phys. Rev. B **104**, 195404 (2021).

[35] Z. He and H. Weng, npj Quantum Mater. **6**, 101 (2021).

[36] A. Chakraborty, K. Das, S. Sinha, P. C. Adak, M. M. Deshmukh, and A. Agarwal, 2D Mater. **9**, 045020 (2022).

[37] A. Bandyopadhyay, N. B. Joseph, and A. Narayan, 2D Mater. **9**, 035013 (2022).

[38] T. Ma, H. Chen, K. Yananose, X. Zhou, L. Wang, R. Li, Z. Zhu, Z. Wu, Q.-H. Xu, J. Yu, C. W. Qiu, A. Stroppa, and K. P. Loh, Nat. Commun. **13**, 5465 (2022).

[39] J.-S. You, S. Fang, S.-Y. Xu, E. Kaxiras, and T. Low, Phys. Rev. B **98**, 121109(R) (2018).

[40] J. Son, K.-H. Kim, Y. H. Ahn, H.-W. Lee, and J. Lee, Phys. Rev. Lett. **123**, 036806 (2019).

[41] R.-C. Xiao, D.-F. Shao, Z.-Q. Zhang, and H. Jiang, Phys. Rev. Appl. **13**, 044014 (2020).

[42] R.-C. Xiao, D.-F. Shao, W. Huang, and H. Jiang, Phys. Rev. B **102**, 024109 (2020).

[43] M.-S. Qin, P.-F. Zhu, X.-G. Ye, W.-Z. Xu, Z.-H. Song, J. Liang, K. Liu, and Z.-M. Liao, Chin. Phys. Lett. **38**, 017301 (2021).

[44] K.-H. Jin, E. Oh, R. Stania, F. Liu, and H. W. Yeom, Nano Lett. **21**, 9468 (2021).

[45] J. Lu, O. Zheliuk, I. Leermakers, N. F. Yuan, U. Zeitler, K. T. Law, and J. Ye, Science **350**, 1353 (2015).

[46] Y. Saito, Y. Nakamura, M. S. Bahramy, Y. Kohama, J. Ye, Y. Kasahara, Y. Nakagawa, M. Onga, M. Tokunaga, T. Nojima, Y. Yanase, and Y. Iwasa, Nat. Phys. **12**, 144 (2016).

[47] X. Xi, Z. Wang, W. Zhao, J.-H. Park, K. T. Law, H. Berger, L. Forró, J. Shan, and K. F. Mak, Nat. Phys. **12**, 139 (2016).

[48] Y. Xing, K. Zhao, P. Shan, F. Zheng, Y. Zhang, H. Fu, Y. Liu, M. Tian, C. Xi, H. Liu, J. Feng, X. Lin, S. Ji, X. Chen, Q.-K. Xue, and J. Wang, Nano Lett. **17**, 6802 (2017).

[49] M. Smidman, M. Salamon, H. Yuan, and D. Agterberg, Rep. Prog. Phys. **80**, 036501 (2017).

[50] W. Li, J. Huang, X. Li, S. Zhao, J. Lu, Z. V. Han, and H. Wang, Mater. Today Phys. **21**, 100504 (2021).

[51] J. Chen, D. Xie, W. Zhou, Q. Xia, and F. Ouyang, Comput. Mater. Sci. **192**, 110411 (2021).

[52] J. Cui, P. Li, J. Zhou, W.-Y. He, X. Huang, J. Yi, J. Fan, Z. Ji, X. Jing, F. Qu, Z. G. Cheng, C. Yang, L. Lu, K. Suenaga, J. Liu, K. T. Law, J. Lin, Z. Liu, and G. Liu, Nat. Commun. **10**, 2044 (2019).

[53] A. B. Maghirang III, G. Macam, A. Sufyan, Z.-Q. Huang, C.-H. Hsu, and F.-C. Chuang, Chin. J. Phys. **77**, 2346 (2022).

[54] W. Kohn and L. J. Sham, Phys. Rev. **140**, A1133 (1965).

[55] P. E. Blöchl, Phys. Rev. B **50**, 17953 (1994).

[56] G. Kresse and J. Hafner, Phys. Rev. B **47**, 558 (1993).

[57] G. Kresse and J. Furthmüller, Phys. Rev. B **54**, 11169 (1996).

[58] J. P. Perdew, K. Burke, and M. Ernzerhof, Phys. Rev. Lett. **77**, 3865 (1996).

[59] S. Grimme, J. Comput. Chem. **27**, 1787 (2006).

[60] S. S. Tsirkin, P. A. Puente, and I. Souza, Phys. Rev. B **97**, 035158 (2018).

[61] N. Marzari, A. A. Mostofi, J. R. Yates, I. Souza, and D. Vanderbilt, Rev. Mod. Phys. **84**, 1419 (2012).

[62] A. A. Mostofi, J. R. Yates, G. Pizzi, Y.-S. Lee, I. Souza, D. Vanderbilt, and N. Marzari, Comput. Phys. Commun. **185**, 2309 (2014).

[63] G. Pizzi, V. Vitale, R. Arita, S. Blügel, F. Freimuth, G. Géranton, M. Gibertini, D. Gresch, C. Johnson, T. Koretsune, J. I.-Azpiroz, H. Lee, J.-M. Lihm, D. Marchand, A. Marrazzo, Y. Mokrousov, J. I. Mustafa, Y. Nohara, Y. Nomura, L. Paulatto *et al.*, J. Phys.: Condens. Matter **32**, 165902 (2020).

[64] Q. Wu, S. Zhang, H.-F. Song, M. Troyer, and A. A. Soluyanov, Comput. Phys. Commun. **224**, 405 (2018).

[65] F. Giustino, M. L. Cohen, and S. G. Louie, Phys. Rev. B **76**, 165108 (2007).

[66] S. Poncé, E. R. Margine, C. Verdi, and F. Giustino, Comput. Phys. Commun. **209**, 116 (2016).

[67] E. R. Margine and F. Giustino, Phys. Rev. B **87**, 024505 (2013).

[68] See Supplemental Material at http://link.aps.org/supplemental/10.1103/PhysRevB.108.035140 for seven nonequivalent structures based on the relative positions of Mo atoms in the H-Mo$_2$C layer above the T-Mo$_2$C layer, calculated energies of the corresponding seven heterostructures, atomic structures of the semi-infinite slab along the (100) direction of heterostructure I, edge states of the semi-infinite slab for heterostructure I, the electronic band structures calculated without and with SOC of heterostructure II, the phonon spectra of heterostructure II, the $\mathbf{k}$-resolved Berry curvature Ω_z of heterostructure II in the 2D BZ at $E_\mathrm{F} - 0.2$ eV, the distribution of the superconducting gap $\Delta_{n\mathbf{k}}$ at $E_\mathrm{F} + 0.15$ eV for heterostructure II at 5 K, the variation of electron-phonon coupling (EPC) on the Fermi surface, and the spin polarizations calculated with SOC along the S_z direction.

[69] R. Yu, X. L. Qi, A. Bernevig, Z. Fang, and X. Dai, Phys. Rev. B **84**, 075119 (2011).

[70] K. Zhang, N. Zou, Y. Ren, J. Wu, C. Si, and W. Duan, Adv. Funct. Mater. **32**, 2111675 (2022).

[71] J. Lei, A. Kutana, and B. I. Yakobson, J. Mater. Chem. C **5**, 3438 (2017).

[72] J. Bekaert, C. Sevik, and M. V. Milošević, Nanoscale **12**, 17354 (2020).

[73] H.-D. Liu, H.-Y. Lu, N. Jiao, M. Zheng, Y.-P. Li, L. Yang, B. Wang, and P. Zhang, Phys. Chem. Chem. Phys. **25**, 580 (2022).

[74] X.-L. Qi and S.-C. Zhang, Rev. Mod. Phys. **83**, 1057 (2011).